

Numerical analysis of a planar anode-supported SOFC with composite electrodes

Thin X. Ho ^{a,*} Pawel Kosinski ^a Alex C. Hoffmann ^a

Arild Vik ^b

^a*Department of Physics and Technology, University of Bergen,*

Allegt 55, 5007 Bergen, Norway

^b*Prototech AS, Fantoftvegen 38, 5892 Bergen, Norway*

Abstract

This paper investigates a planar anode-supported solid oxide fuel cell (SOFC) with mixed-conducting electrodes. Direct internal methane reforming in the high-temperature cell is included. The numerical model used is in principle three-dimensional, a single computational domain comprising the fuel and air channels and the electrodes–electrolyte assembly. The oxygen ion transport through the electrolyte is mimicked with an algorithm for Fickian diffusion built into the commercial computational package Star-CD. The equations describing transport, chemical and electrochemical processes for mass, momentum, species and energy are solved using Star-CD with in-house developed subroutines. Results for temperature, chemical species and current density distribution for co- and counter-flow configurations are shown and discussed. For co-flow, a sub-cooling effect manifests itself in the methane-rich region near the fuel entrance, while for counter-flow a super-heating effect manifests

itself somewhat further downstream, where all the methane is consumed. Effects of varying air inlet conditions are also investigated.

Key words: SOFC; Modeling; Composite electrode; Transport process; Charge transport

Nomenclature

A_{ac}	active area per unit volume, m^{-1}
c	constant-volume specific heat, J kg^{-1}
C	effective concentration, C m^{-3} or $F\text{mole m}^{-3}$
C_i	oxygen ion concentration, mol m^{-3}
d_p	pore diameter, m
D	diffusion coefficient, $\text{m}^2 \text{s}^{-1}$
e	specific internal energy, $\text{J kg}^{-1} \text{K}^{-1}$
E	potential, V
f	unit conversion constant
F	Faraday constant, 96487 C mol^{-1}
$F_{m,j}$	diffusive mass flux of species m , $\text{kg m}^{-2} \text{s}^{-1}$
$F_{h,j}$	diffusive energy flux component, $\text{J m}^{-2} \text{s}^{-1}$
h_t	thermal enthalpy, $\text{J kg}^{-1} \text{K}^{-1}$
$h_{t,m}$	thermal enthalpy of species m , J kg^{-1}
i	transfer current per unit volume, $\text{C m}^{-3} \text{s}^{-1}$
i_0	exchange current density, $\text{C m}^{-2} \text{s}^{-1}$

* Corresponding author. Tel: +47 55 57 41 28; Fax: +47 55 57 41 14

Email address: think.ho@ift.uib.no (Think X. Ho)

k	thermal conductivity, $\text{W m}^{-1} \text{K}^{-1}$
$k_{0,a}, k_{0,c}$	reaction rate coefficient, $\text{mole m}^{-3} \text{s}^{-1} \text{V}^{-1}$
K_i	permeability of porous media, $\text{kg m}^{-3} \text{s}^{-1}$
M	molecular weights, g mol^{-1}
n	number of electrons, 2
p	pressure, Pa
r	reaction rate, $\text{mole m}^{-3} \text{s}^{-1}$
R	universal constant of gas, $8.314 \text{ J kg}^{-1} \text{K}^{-1}$
R_{ref}	reforming reaction rate, $\text{mole m}^{-3} \text{s}^{-1}$
s_c	chemical energy source, $\text{J m}^{-3} \text{s}^{-1}$
s_h	energy source, $\text{J m}^{-3} \text{s}^{-1}$
s_i	momentum source component, $\text{kg m}^{-2} \text{s}^{-2}$
s_m	production/consumption rate of species m , $\text{kg m}^{-3} \text{s}^{-1}$
T	temperature, K
u_i	velocity component, m s^{-1}
U_i	superficial velocity component, m s^{-1}
W_{Ni}	nikel load, g m^{-3}
x_i	Cartesian coordinate, m
Y_m	mass fraction of component m

Greek letters

β	symmetry factor, 0.5
ϵ	porosity
η	overpotential, V
λ	ionic conductivity, $\Omega^{-1} \text{m}^{-1}$
μ	dynamic viscosity of gas, $\text{kg m}^{-1} \text{s}^{-1}$

Φ	potential, V
ρ	gas mixture density, kg m ⁻³
τ	tortuosity
τ_{ij}	stress tensor, Pa

Subscripts

m, n	species index
a	anode active layer
c	cathode active layer
e	electronic phase
i	ionic phase
i, j, k	Cartesian directions
rev	reversible

Abbreviations

ACC	anode current collector
ACL	anode catalyst layer
CCC	cathode current collector
CCL	cathode catalyst layer

1 Introduction

Solid oxide fuel cells (SOFCs), which generate electricity directly from fuel in an electrochemical process at high temperature, possess some advantages even compared to other types of fuel cells: high efficiency and the capability of working with a relatively wide range of fuels. A typical solid oxide fuel cell

(SOFC) can work with pure hydrogen, methane or natural gas. Direct internal reforming normally with steam, gives rise to a high efficiency since the heat generated by electrochemical processes can be used for the in situ endothermic reforming reactions. This reduces the need for pre-reforming and cell cooling by extra air passing to the cathode side of the cell, lowering the costs.

In state-of-the-art SOFC installations, tubular and planar cells are the most common designs. Tubular design has the advantage that sealing is easier. However, the planar design, as we consider here, is superior in terms of efficiency and ease of manufacture and stacking. There have been a few publications dealing with the performance of planar SOFCs working with hydrogen [1–3] or with methane internal reforming [4,5]. We describe these in a bit more detail below, the cell performance is a complex function of the cell designs, the materials, the nature of fuels and the operating conditions.

Pramuanjaroenkij et al. [1] recently presented a 2D model for analyzing the performance of a planar SOFC fed by H_2 mixed with H_2O to the anode channel. The co-flow configuration was considered. With the electrolyte material of yttria-stabilized zirconia, a cell with anode-supported design was shown to give higher power density in the high current density range than that with electrolyte-supported design at $800^\circ C$. Chaisantikulwat et al. [2] modeled the dynamic behavior of a repeating unit cell as a consequence of step changes in the load current and input hydrogen concentration. Recknagle et al. [3] presented a Star-CD–based–3D model for predicting the distribution of temperature and current density in a planar SOFC stack with three flow configurations, working with H_2 as fuel. It was found that the co-flow configuration generates the most uniform temperature and thus the smallest temperature gradients.

Aguiar et al. [4] investigated the performance of an anode-supported SOFC with direct internal reforming for co- and counter-flow configurations. The results showed that with the same fuel and air inlet conditions, the counter-flow configuration gave rise to the least optimal operation due to steep temperature gradients and uneven current density distributions. However, the model used was one-dimensional and was for the cell working at intermediate temperatures (650–800°C). Nikooyeh et al. [5] presented a 3D model where the steam-to-carbon ratio, which is known to determine the propensity for carbon to deposit on the anode cermet, was evaluated. However, it remained unclear where exactly in the anode the heat generated by the electrochemical reactions should be applied.

In most of the mentioned models, micro-processes occurring in the porous electrodes are either ignored or modeled by empirical correlations while considering the whole positive electrode–electrolyte–negative electrode (PEN) structure a single solid component without thickness. Electrochemical processes are simply implemented via current density as boundary conditions at the electrodes–electrolyte interface. Moreover, the output voltage is mostly derived from the Nernst potential subtracting irreversibilities estimated from empirical correlations. A good review of numerical modeling of SOFCs can be found in [6].

In this paper we use a detailed model for a planar anode-supported SOFC with composite electrodes. Direct internal reforming of methane with steam is included. Carbon monoxide produced by the reforming reaction takes part in the electrochemical processes while being in equilibrium with the water-gas shift reaction. The porous cermet electrodes and the electrolyte membrane are meshed to capture all the micro-processes including the chemical and electro-

chemical processes, the transport of gas species in the pores, the transport of heat due to the chemical and electrochemical processes and the transport of charge. The model is three-dimensional in principle. The Nernst potential is not used to derive the operating voltage. Rather, it is fixed by imposing a constant potential on each of the electrodes.

2 Model description

2.1 Domain of consideration

Figure 1 shows a schematic diagram of the model with abbreviations ACC and CCC denoting the anode and cathode current collectors, respectively, and ACL and CCL denoting the anode and cathode catalyst layers, respectively. The dashed lines indicate the modeling domain, which does not include the interconnects at this stage limiting the computational cost.

[Fig. 1 about here.]

The catalyst (active) layers consist of binary mixtures of, respectively, electron and ion conducting particles building up three-phase boundaries where the electrochemical processes take place. These electrochemically active sites are assumed to be continuous and homogeneous. The catalyst layers are very thin (10–30 μm), especially when compared to the total anode thickness ($\sim 630 \mu\text{m}$) in the anode-supported SOFC design. The current collectors collect electrons and ensure uniform diffusion of chemical species away from or to the electrochemically active sites. The anode current collector is also a region where the catalyzed methane reforming reactions mostly take place.

In the present paper ideal gas mixtures are assumed. Additionally, the gas channel flows are assumed to be incompressible and laminar. This is supported by the low rates of generation and/or consumption of gas species, the small pressure gradients and the low Reynolds numbers.

2.2 Modeling of mass and heat transfer

In this part we present the system of equations for mass, species and energy transport chosen from the commercial package Star-CD [7]. These will be solved on the computational domain described above. The Einstein summation convention is employed with subscripts i and j denoting Cartesian coordinates.

2.2.1 Fluid flow

The fluid flow field is governed by the mass conservation equation:

$$\frac{\partial \epsilon \rho}{\partial t} + \frac{\partial \rho u_j}{\partial x_j} = 0 \quad (1)$$

and the momentum equation of which the i th component is

$$\frac{\partial \rho u_i}{\partial t} + \frac{\partial}{\partial x_j} (\rho u_j u_i - \tau_{ij}) = -\frac{\partial p}{\partial x_i} + s_i \quad (2)$$

where ϵ is the porosity the value of which varies between regions i.e. it is unity in the gas channels, a value between 0 and 1 in the electrodes and approximately 0 in the electrolyte, ρ the gas mixture density, u_i the velocity component in direction x_i , p the pressure, s_i the i th momentum source component and τ_{ij} the stress tensor.

In the porous electrodes and the electrolyte membrane, the latter of which is also considered a porous medium with approximately zero porosity in the

present model, the momentum balance in Eq. (2) is replaced by an equation for gas permeation:

$$\frac{\partial p}{\partial x_i} = -K_i U_i \quad (3)$$

where U_i is the superficial velocity in direction x_i , defined as the volume flow rate divided by the total cross sectional area and $K_i = \alpha_i |u| + \beta_i$ the resistance with the coefficients α_i and β_i are assumed to have the same values in the three different orthogonal directions and given as [8]

$$\alpha = \frac{1.75\rho(1-\epsilon)}{\epsilon^3 d_p}; \quad \beta = \frac{150\mu(1-\epsilon)^2}{\epsilon^3 d_p^2}, \quad (4)$$

which is consistent with the Ergun equation for flow through a bed of particles. Here, d_p is the pore diameter and μ the dynamic viscosity of the gas mixture.

2.2.2 Mass transfer

In order to resolve the species balance, the following species transport equation is used:

$$\frac{\partial \epsilon \rho Y_m}{\partial t} + \frac{\partial}{\partial x_j} (\rho u_j Y_m + F_{m,j}) = s_m \quad (5)$$

where Y_m is the mass fraction of species m , s_m the rate of mass production/consumption of species m per unit volume due to chemical and/or electrochemical reactions and $F_{m,j}$ the diffusive mass flux of species m , which is modeled using Fick's law:

$$F_{m,j} = -\rho D_{m,j} \frac{\partial Y_m}{\partial x_j} \quad (6)$$

where $D_{m,j}$ is the diffusion coefficient of species m , which in an isotropic material has the same value in all directions and is determined as a combination of ordinary and Knudsen diffusion:

$$\frac{1}{D_m} = \frac{1}{D_{mn}} + \frac{1}{D_{mK}} \quad (7)$$

where D_{mn} is the ordinary binary diffusion coefficient of species m in species n and D_{mK} the Knudsen diffusion coefficient of species m . These are calculated by [8]

$$D_{mn} = 1.858 \cdot 10^{-7} \sqrt{\frac{1}{M_m} + \frac{1}{M_n}} \frac{T^{3/2}}{p \sigma_{mn}^2 \omega_D} \quad (8)$$

$$D_{mK} = \frac{d_p}{3} \sqrt{\frac{8RT}{\pi M_m}} \quad (9)$$

Here, M_m and M_n are the molecular weights (g mol^{-1}) of species m and n respectively, p the total pressure (atm), σ_{mn} and dimensionless ω_D are Lennard-Jones parameters, T the temperature (K) and R the universal constant of gas ($\text{J kg}^{-1} \text{K}^{-1}$).

However, in porous media an effective diffusion coefficient, D_m^{eff} , is used. It is a modification of D_m in order to take into account the structural parameters such as the tortuosity, τ , and the porosity, ϵ , by $D_m^{\text{eff}} = (\epsilon/\tau) D_m$.

2.2.3 Heat transfer

The enthalpy equation for a solid or fluid of constant density is:

$$\frac{\partial}{\partial t} (\epsilon \rho e) + \frac{\partial}{\partial x_j} (\rho u_j e + F_{h,j}) = \tau_{ij} \frac{\partial u_i}{\partial x_j} + s_h - s_c \quad (10)$$

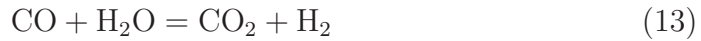
where $e = \bar{c}T - c_0 T_0$ is the specific internal energy, s_h the energy source due to e.g. ohmic resistances and radiation, s_c the chemical energy source accounting for endo- or exo-thermic chemical and electrochemical processes. The diffusive thermal flux, $F_{h,j}$, is the combination of Fourier's conduction and the heat transported by diffusive mass fluxes, defined as:

$$F_{h,j} = -k \frac{\partial T}{\partial x_j} + \sum_m h_{t,m} F_{m,j} \quad (11)$$

where k is the thermal conductivity of gas mixture or solid materials and $h_{t,m}$ the specific enthalpy of species m . Note that parameters are chosen appropriately for different regions. For example, when solving Eq. (10) for solid regions, the terms that contain velocity in Eq. (10) and the second term on the right side of Eq. (11) vanish.

2.3 Modeling of chemistry

Endothermic internal reforming of methane can be utilized to provide additional cooling of the fuel cell and to reduce the expense of pre-reforming. The steam methane reforming and water-gas shift reactions are, respectively



The reforming reaction is supposed to occur on the surface of nickel particles which are mixed with yttria-stabilized zirconia (YSZ) particles and function as an electronic conductor on the anode side. The mechanism of the reaction on the Ni-surface is a complex process [9,10], which is beyond the scope of this work. Rather its kinetics is given as a function of nickel load based on the single step reaction mechanism as [11]

$$R_{ref} = 1.75 \left(\frac{p_{\text{CH}_4}}{101325} \right)^{1.2} W_{\text{Ni}} \exp \left(\frac{-57840}{RT} \right) \quad (14)$$

where R_{ref} ($\text{mol m}^{-3} \text{s}^{-1}$) is the reforming reaction rate, p_{CH_4} (Pa) the partial pressure of methane and W_{Ni} the nickel load (g m^{-3}).

The adsorption of reactants on and the desorption of products from the Ni-surface are crucial processes of the reaction mechanism. The availability of

free surface of Ni-particles should, therefore, contribute to the reaction kinetics. With the anode-supported design, the reforming mostly takes place in the anode current collector. However, nickel particles are also present in the anode active layer, which has a thickness of 30 μm in our model. This may probably stimulate the reforming reaction. However, since the hydrogen oxidation electrochemically takes place on the three-phase boundaries of the active layer, a competition among different species in reaching and/or leaving the nickel surface may exist. As a result, the reforming rate may be lower as the available free surface of Ni-particles lower. It is here assumed to be two orders lower in this layer compared to that in the anode current collector. Additionally, at high operating temperature (800–1000°C) of the cell, steam methane reforming can probably occur directly in the gas phase, although it has been found to be only little at temperatures below 800°C [12]. A rate of three orders of magnitude lower than that in the current collector is therefore proposed for the reforming reaction in the fuel channel.

The water-gas shift reaction is kinetically fast and therefore assumed to be at equilibrium. CO produced by the reforming reaction can probably both shifted towards producing further H₂ and CO₂ and oxidized at the three-phase boundaries producing electricity and CO₂. Peters et al. [13] has experimentally shown that the concentration of CO is somewhat higher than that given by the shift reaction equilibrium. This is probably caused by the presence of methane throughout the system. The in situ fast and continuous production of CO by the methane reforming reaction prevents the shift reaction from reaching its equilibrium state. However, in our system methane is quickly consumed near the fuel entrance [14], leaving most of the anode part empty of methane. Therefore, there will probably be enough time for CO to reach its equilibrium

concentration. The equilibrium state of the shift reaction is controlled by the equilibrium constant, K . The shift reaction will run forward in case $K > (p_{\text{CO}_2}p_{\text{H}_2})/(p_{\text{CO}}p_{\text{H}_2\text{O}})$, producing further CO_2 and H_2 while consuming CO and H_2O , and runs backward in the opposite case.

Carbon formation on the Ni-YSZ cermet anode, which impedes gas flow and blocks active sites on the anode, is neglected since the steam-to-carbon ratio is high.

2.4 Modeling of electrochemistry

2.4.1 Electrochemical reactions

Oxygen is reduced at the three-phase boundaries in the cathode catalyst layer producing oxygen ions. The reduction reaction is given as



The oxidation reactions of H_2 and CO at the three-phase boundaries in the anode catalyst layer are given, respectively, as



The cell reactions are



The half-cell reactions of Eqs. (15), (16) and (17) can be written in short as



The relation between the transfer current, which is defined by the difference in current given by the forward and backward reactions of Eq. (20), and the activation overpotentials is given by the Butler–Volmer equation [15,16]:

$$i = A_{ac}i_0 \left\{ \exp\left(\beta \frac{nF\eta}{RT}\right) - \exp\left[-(1 - \beta) \frac{nF\eta}{RT}\right] \right\} \quad (21)$$

Here, i and A_{ac} are the transfer current and the electrochemically active area per unit volume of the catalyst layers. i_0 is the exchange current density, β the transfer coefficient or the symmetry factor, which can be taken as 0.5 for fuel cell applications, $n = 2$ is the number of electrons participating in the electrochemical reactions, F is Faraday’s constant and η the activation overpotential. We note that when based on the reversible reaction of Eq. (20) i is positive for the anode side where the oxidation of H_2 and CO is dominant and negative for the cathode side where the reduction of O_2 is dominant.

Although CO mostly participates in the water-gas shift reaction of Eq. (13) rather than in the electrochemical processes [17], the oxidation reaction of CO does occur and is therefore included in our model in order to make it more realistic and general. In a system where H_2 and CO coexist, the rate of CO oxidation is around 2–3 times less than that of H_2 oxidation depending on the operating temperature [18]. In our model, a rate of CO oxidation of 3 times less than that of H_2 oxidation is adopted, since most of the cell is at high temperature (800–1000°C).

We note that methane can possibly be electrochemically oxidized in case of absence (or near-absence) of steam at the feed [19,20]. However, in this work with high content of steam at the feed, the fast reforming reaction will dominate over any oxidation of methane. Methane electrochemical oxidation is, therefore, ignored in this work. It is good to note that the oxidation of CO

and H_2 produces the same Nernst potential in the cell since the water-gas shift reaction is at equilibrium [21]. Therefore, in the rest of this paper, the electromotive force calculation is based solely on H_2 .

2.4.2 Activation overpotential

The activation overpotential for an electrode is defined as

$$\eta = (\Phi_e - \Phi_i) - (\Phi_e - \Phi_i)_{\text{eq}} \quad (22)$$

where Φ_e and Φ_i are the electric potential of the electronic (electrode) and ionic (electrolyte) phases, respectively. The subscript eq denotes the equilibrium state. The potential difference at equilibrium is actually the reversible potential of an electrode, i.e. $(\Phi_e - \Phi_i)_{\text{eq}} = E_{\text{rev}}$. The reversible potentials for the cathode and anode are given, respectively, as e.g. [22]

$$E_{\text{rev,c}} = \frac{1}{4F} (\mu_{\text{O}_2} - 2\mu_{\text{O}_c^{-2}}) \quad (23)$$

$$E_{\text{rev,a}} = \frac{1}{2F} (\mu_{\text{H}_2\text{O}} - \mu_{\text{H}_2} - \mu_{\text{O}_a^{-2}}) \quad (24)$$

where μ_i is the chemical potential of species i , which is defined as $\mu_i = \mu_i^0 + RT \ln p_i$ for ideal gases.

At open circuit conditions, the net current flux through the electrolyte, which is the combination of transports due to leaking electrons and ions, vanishes. With YSZ electrolyte materials, the electronic leakage current is negligible, hence the transport of oxygen ions from the cathode to the anode side at open circuit conditions is also negligible [23]. Therefore, it is reasonable to assume that $\mu_{\text{O}_c^{-2}} = \mu_{\text{O}_a^{-2}}$, the reversible potential of the cell or the Nernst

potential is thus obtained by combining the electrode reversible potentials

$$\begin{aligned} E_{\text{rev}} &= E_0 + \frac{RT}{2F} \ln \left(\frac{p_{\text{H}_2, \text{a}}}{p_{\text{H}_2\text{O}, \text{a}}} \right) + \frac{RT}{4F} \ln p_{\text{O}_2, \text{c}} \\ &= E_{\text{rev}, \text{c}} - E_{\text{rev}, \text{a}} \end{aligned} \quad (25)$$

where the Nernst potential under standard conditions $E_0 = -\Delta G^0/2F$ with $\Delta G^0 = \mu_{\text{H}_2\text{O}}^0 - \mu_{\text{H}_2}^0 - \mu_{\text{O}_2}^0/2$ the standard Gibbs free energy change of the cell reaction based, as mentioned above, on H_2 oxidation only.

The determination of the electrode reversible potentials depends upon an applied reference potential. By choosing the reference potential as $-(\mu_{\text{O}_2}^0 - 2\mu_{\text{O}_c^-})/4F$, the reversible potentials for cathode and anode given by Eqs. (23) and (24) become, respectively, as [14]

$$E_{\text{rev}, \text{c}} = \frac{RT}{4F} \ln p_{\text{O}_2} \quad (26)$$

$$E_{\text{rev}, \text{a}} = -E_0 + \frac{RT}{2F} \ln \left(\frac{p_{\text{H}_2\text{O}}}{p_{\text{H}_2}} \right). \quad (27)$$

A linear approximation of the Butler–Volmer equation (Eq. (21)), which is obtained by using the truncated Taylor series $e^x \approx 1 + x$ when the activation overpotential η is small is adopted in the present paper. Therefore, the kinetics of the half-cell reactions can be calculated by

$$r = k_0 |\eta|. \quad (28)$$

Here, $r = |i|/F$ is the reaction rate of the half-cell reactions, given in $\text{mol m}^{-3} \text{s}^{-1}$ and the coefficient k_0 is defined as $k_0 = 2A_{\text{ac}}i_0/RT$. We note that r is the reduction reaction rate of O_2 at the cathode active layer and the total oxidation reaction rates of H_2 and CO at the anode active layer.

Consequently, from Eqs. (22), (26) and (27), Eq. (28) for cathode half-cell

reaction and total anode half-cell reactions become, respectively:

$$r_c = - \left[(\Phi_{e,c} - \Phi_{i,c}) - \frac{RT}{4F} \ln p_{O_2} \right] k_{0,c} \quad (29)$$

$$r_a = \left[(\Phi_{e,a} - \Phi_{i,a}) + E_0 - \frac{RT}{2F} \ln \left(\frac{p_{H_2O}}{p_{H_2}} \right) \right] k_{0,a} \quad (30)$$

where $k_{0,c}$ and $k_{0,a}$ are the rate coefficients for the cathode and anode reactions, respectively. These depend upon the exchange current density and the electrochemically active area per unit volume of the catalyst layers.

2.4.3 Charge transfer

Details of the charge transfer approach have been presented elsewhere [14]. However, it is briefly reviewed in this section. The transport of oxygen ions across the electrolyte membrane can be given by the Nernst–Planck equation, as

$$i = -DzF \left(\frac{\partial C_i}{\partial x} + zC_i \frac{F}{RT} \frac{\partial \Phi_i}{\partial x} \right) \quad (31)$$

where i ($C \text{ m}^{-2} \text{ s}^{-1}$) is the current density due to the flow of oxygen ions, C_i (mol m^{-3}) the oxygen ion concentration, $z = 2$ the valence of oxygen ions and Φ_i (V) the electric potential of the ionic phase. The physical meanings of the two terms in the Eq. (31) are well understood, the first term represents the contribution due to any concentration gradient of oxygen ions and is in the form of Fick’s first law, and the second term represents the contribution due to any electric potential gradient. Note that there is no convection term in the Nernst-Planck equation for SOFCs.

In case of absence of a concentration gradient, as for SOFCs when oxygen ion concentration is high and almost uniform, the diffusion term will vanish. The

transport of ions, as a consequence, becomes ohmic and can be written as

$$i = D \frac{\partial}{\partial x} \left(-C_i \frac{z^2 F^2}{RT} \Phi_i \right) = D \frac{\partial C}{\partial x} \quad (32)$$

where $C = -C_i \frac{z^2 F^2}{RT} \Phi_i$ is an "effective concentration" representing the ionic potential in the electrolyte.

Equation (32) has the form of Fickian diffusion, an algorithm for which is built in the commercial computational package Star-CD. Note that the current density by convention is defined as the flux of positive charge. Therefore a minus sign will appear in front of D when applied to flux of oxygen ions. In the present paper we use the in-built Fickian model of Star-CD to model the flux of oxygen ions across the electrolyte. However, the coefficient D is not used at least at this stage as a physical diffusion coefficient. It is fitted instead and the so-called "effective diffusion coefficient" thus used to obtain realistic results. In order to do that, a simple unit conversion constant, f , is introduced, i.e. $dC = f d\Phi_i$ and f takes on the value -1 if C is in $F\text{mol m}^{-3}$, and -96487 if C is in C m^{-3} . Consequently, Ohm's law for the ion transport across the electrolyte can be written as

$$i = -\lambda \frac{\partial \Phi_i}{\partial x} = -\frac{\lambda}{f} \frac{\partial C}{\partial x} \quad (33)$$

where λ is the ionic conductivity of the electrolyte material. Comparing Eq. (32) with Eq. (33), the so-called effective diffusion coefficient is determined by $D = -\lambda/f$.

2.4.4 Cell voltage

The operating cell voltage can be determined by the electric potential difference between cathode and anode current collectors [14,24]. In case of large

electrical conductivity of electrode materials, constant electric potentials can be assumed throughout the electrodes including the catalyst layers and this is done here. The operating cell voltage is therefore uniform along the cell length and given by

$$E_{\text{cell}} = \Phi_{e,c} - \Phi_{e,a} \quad (34)$$

where $\Phi_{e,c}$ and $\Phi_{e,a}$ are the electric potentials of the electronic phase in the cathode and anode active layers, respectively. They can take on the values -1.0 V and -1.7 V, respectively, for instance, for a cell voltage of 0.7 V.

At steady state, the rate of oxygen ion production at the cathode active layer, given by Eq. (29), balances with the rate of consumption at the anode active layer given by Eq. (30). The current density will be obtained using Eq. (32) connecting the flux of oxygen ions produced on one side and consumed on the other side of the electrolyte. In the present model, an iterative method is used to solve for Φ_i in the active layers and the electrolyte. Subroutines built in-house are used to handle these balances.

3 Computational mesh

The computational domain is continuous and consists of the two gas channels, the current collectors, the catalyst layers and the electrolyte membrane, which hereinafter are called subdomains (see Fig. 1). Uniform meshes for the finite volume method are generated in each subdomain. Dimensions of cell components and the number of computational elements in each subdomain can be found in Table 1. Figure 2 shows the computational mesh used. In the z -direction, since there is only one element being generated the model functions as a two-dimensional one even though all mathematical equations were

developed for a generic three-dimensional problem. It is good to note that the simulated results do not depend on the mesh size [14].

[Fig. 2 about here.]

[Table 1 about here.]

4 Results and discussion

4.1 Model parameters

Methane is pre-reformed prior to feeding into the anode channel by steam with steam-to-carbon ratio of 2.5 at 800°C. The fraction of methane converted in the pre-reforming process is 30%, meaning that most of the methane is still flowing into the cell. The water-gas shift reaction is assumed to be at equilibrium in the pre-reformer. Fuel compositions and other boundary and operating conditions can be found in Table 2. The physical properties of the cell components are shown in Table 3. These parameters are used for both co- and counter-flow cases, however, for the latter the inlet velocity of the air takes on negative values.

[Table 2 about here.]

[Table 3 about here.]

4.2 Co-flow configuration

Figure 3 presents the concentration profiles of the chemical species in the anode channel along the cell length. We note that the Star-CD post-processing tools can show in color scales the profiles of every single quantity. However, we prefer to use numbers due to advantages that they allow us to see in higher resolution and to plot many species together in a single figure for comparison. Therefore, in this paper, all the results are plotted based on the data exported from Star-CD using in-house developed subroutines. The mean temperature of the bulk-gas channels and the electrolyte membrane along the cell length is shown in Figure 4.

As can be seen in Figure 3, methane is quickly consumed so that most of the anode compartment is methane free. The concentration of H_2 and CO increases commensurate with the consumption of CH_4 . The fast reaction of CH_4 consumes a large amount of heat, cooling down the cell locally near the entrance of the cell (see Figure 4). Obviously, the sub-cooling effect occurs in the area where CH_4 is still present in significant amounts. However, the oxidation of H_2 and CO , for the latter in parallel with the shift reaction, produces heat at the anode catalyst layer maintaining the cell at the temperatures required for an acceptably high ionic conductivity in the electrolyte material. Fuel utilization is 62.8% and the stoichiometry factor or air ratio, which is the molar ratio between the air supplied to the cell and the air needed for stoichiometric electrode reactions, is approximately 10.6 in this case.

[Fig. 3 about here.]

[Fig. 4 about here.]

Simulations where the oxidation of CO is neglected were also performed. For these, all parameters are kept the same as for the base case with CO oxidation included. Results of the temperature in the electrolyte membrane and the current density are shown in Figures 5 and 6, respectively, and compared with those obtained from the base case. The temperature and current density obtained from the base case with CO oxidation are slightly higher than those obtained from the case with CO oxidation neglected. This can be explained by the fact that the heat released from CO oxidation is higher than that from H₂ oxidation. The enthalpy of reaction is approximately $-282.47 \text{ kJ mol}^{-1}$ for CO oxidation, while it is $-248.42 \text{ kJ mol}^{-1}$ for H₂ oxidation at 1073 K. The results are in line with experimental findings by [19] that there is no significant difference on the cell performance with pure H₂ and with a mixture of 25% CO and 75% H₂. The difference in temperature between the two cases is less than 1 K as shown in Figure 5. The current-density profiles exhibit a low region corresponding to the sub-cooling area, which impedes the transport of oxygen ions through the electrolyte membrane. The current goes down somewhat at the outlet where fuel starts to deplete. The average current density is 0.55 A cm^{-2} , yielding a power density of 0.385 W cm^{-2} .

[Fig. 5 about here.]

[Fig. 6 about here.]

4.3 Counter-flow configuration

The same inlet conditions and physical parameters as for the co-flow case are kept for the counter-flow case. All parameters can be found in Tables 2 and

3. However, the air inlet velocity is given a negative value, i.e. -6.3 m/s in this case. This simulation case for counter-flow is considered the base case and will be used for comparison with other simulations with varying air inlet conditions. Figure 7 represents the gas species compositions in the bulk-gas anode channel along the cell length. These values are averaged across the thickness of the channel. It can be seen that CH_4 is consumed faster than in the co-flow case. The consumption of H_2 and CO is also faster, corresponding to a fuel utilization of 83.9% which is higher than that for the co-flow case.

[Fig. 7 about here.]

The mean temperature of the bulk-gas air and fuel channels and the electrolyte membrane is presented in Figure 8. Unlike the co-flow case, the temperature profiles of the counter-flow case show a peak near the fuel entrance. This super-heating effect is caused by the heat generated by the electrochemical processes. The transport of heat by convection probably plays an important role in determining where along the cell length the peak manifests itself. The velocity of the air stream in the air channel is much greater than that of the fuel stream in the fuel channel. This is likely why the peak is brought downstream with respect to the air flow. However, the super-heating zone is positioned somewhat further in the fuel stream direction than the peak in the H_2 profile (Figure 7) where all CH_4 is reacted away. This is the effect due to the endothermic reforming reaction consuming the heat as long as CH_4 is still present in significant amounts. The calculated stoichiometry factor is a bit lower and approximately equal to 7.6.

[Fig. 8 about here.]

The current density calculated based on the flux of oxygen ions through the electrolyte is shown in Figure 9. A peak in the current density profile is also seen. Its position is between the positions of the peaks in the H_2 and the temperature profiles, since the current density depends on both the temperature and the content of H_2 and probably CO. The low current-density zone near the exit of the fuel is due to fuel depletion as fuel utilization is high in this case. The cell average current density is 0.76 A cm^{-2} , resulting in an electrical power density of 0.532 W cm^{-2} , higher than that given by the co-flow case. In short, compared to the co-flow configuration with the same air and fuel inlet conditions, the counter-flow case gives a higher power density and thus fuel efficiency. Higher overall temperatures in the cell and higher temperature gradients are, however, also consequences of the higher power density and are not favorable from the material viewpoint.

[Fig. 9 about here.]

4.3.1 *Effect of the air inlet temperature*

The super-heating effect giving rise to high thermal stresses and highly non-uniform distribution of the current density should be reduced to make possible to operate the cell with this flow configuration. To achieve this, the inlet temperature of the air is decreased to 1023 K. All other parameters are kept the same as for the base case presented above. Results for the electrolyte temperature and current density are compared with those of the base case in Figures 10 and 11, respectively.

[Fig. 10 about here.]

[Fig. 11 about here.]

With the lower inlet temperature of the air, the super-heating effect is reduced with a lowering of the maximum temperature by around 92 K. Moreover, a decrease of around 36 K in the maximum overall temperature difference is obtained. It can be seen in Figure 11 that the current density profile is more uniform than that in the base case. However, since the overall cell temperature decreases, the performance of the cell given in terms of the current density decreases. The cell average current density in this case is 0.63 A cm^{-2} . The excess air, as a result, becomes somehow moderate with the stoichiometry factor of 9.6.

4.3.2 Effect of the stoichiometry factor

To check the influence of the stoichiometry factor, the inlet velocity of the air is increased to 8.3 m/s compared to the base case with 6.3 m/s. All other parameters are kept the same as for the base case. Figures 12 and 13 show a comparison between the temperature and current density, respectively, resulting from this case and those from the base case. The simulated stoichiometry factor is 7.6 for the base case and 10.6 for the current case.

[Fig. 12 about here.]

[Fig. 13 about here.]

The maximum temperature and thus the overall temperature difference are reduced considerably (around 51 K) for the case of high air inlet velocity or stoichiometry factor. Moreover, the current density is distributed more uniformly with a small reduction in the average values, i.e. 0.72 A cm^{-2} for the

current case compared to 0.76 A cm^{-2} for the base case. Moreover, with a lower fuel utilization of 79.9% compared to 83.9% with the base case, the current density is slightly higher near the fuel exit due to less depletion of the fuel (see Figure 13).

5 Summary

A planar anode-supported SOFC with composite electrodes was investigated for both the co- and counter-flow configurations. Regarding the fuel compositions, methane is 30% pre-reformed with steam with steam-to-carbon ratio of 2.5 at 800°C before feeding into the SOFC anode. Direct internal reforming therefore takes place in the SOFC anode compartment.

The electrochemical processes occur in the active layers, which are assumed to be homogeneous, with a thickness of $30 \mu\text{m}$ on the anode side and $25 \mu\text{m}$ on the cathode side. The oxidation of CO at the anode active layer was included making the model more realistic. However, the simulated results for the co-flow configuration showed that there is no significant difference in the temperature as well as cell performance between this system and a system where CO oxidation is neglected. This is in line with experimental findings of [19].

With the co-flow case, a sub-cooling effect increasing the local and overall temperature gradients and thus the thermal stresses manifests itself near the entrance of the cell where CH_4 is rich. This is caused by the kinetically strong endothermic reforming reaction. However, with the counter-flow configuration, a super-heating effect occurs again near the fuel entrance but somewhat further

down the fuel stream where all CH_4 is consumed. This effect caused by the accumulated heat of the electrochemical processes makes the cell suffering from high local temperature gradients. Furthermore, higher power density but also higher overall temperature and temperature gradients were obtained with the latter compared to the former at the same fuel and air inlet conditions.

A decrease of 50 K in the air inlet temperature for the counter-flow case can mitigate the high local and overall temperature gradients and lessen the non-uniformity of the current-density profile along the cell length. Similar results were obtained when increasing the inlet velocity of the air from 6.3 m s^{-1} to 8.3 m s^{-1} . These variations of the air inlet conditions make the counter-flow configuration more favorable.

Acknowledgments

Financial support from the NFR through the MSOFC program is gratefully acknowledged.

References

- [1] A. Pramuanjaroenkij, S. Kakac, X. Y. Zhou. Mathematical analysis of planar solid oxide fuel cells. *Int J Hydrogen Energy*. 2008;33(10):2547–65.
- [2] A. Chaisantikulwat, C. Diaz-Goano, E. S. Meadows. Dynamic modelling and control of planar anode-supported solid oxide fuel cell. *Computers & Chemical Engineering* 2008;32:2365–81.
- [3] K. P. Recknagle, R. E. Williford, L. A. Chick, D. R. Rector, M. A. Khaleel.

Three-dimensional thermo-fluid electrochemical modeling of planar SOFC stacks. *J Power Sources* 2003;113:109–14.

- [4] P. Aguiar, C. S. Adjiman, N. P. Brandon. Anode-supported intermediate temperature direct internal reforming solid oxide fuel cell. I: model-based steady-state performance. *J Power Sources* 2004;138:120–36.
- [5] K. Nikooyeh, A. A. Jeje, J. A. Hill. 3D modeling of anode-supported planar SOFC with internal reforming of methane. *J Power Sources* 2007;171(2):601–09.
- [6] S. Kakac, A. Pramuanjaroenkij, X. Y. Zhou. A review of numerical modeling of solid oxide fuel cells. *Int J Hydrogen Energy* 2007;32(7):761–86.
- [7] Star-CD, Version 3.24. Methodology. CD adapco Group; 2004.
- [8] R. B. Bird, W. E. Stewart, E. N. Lightfoot. *Transport phenomena*, 2nd Edition. New York: John Wiley & Sons; 2002.
- [9] E. S. Hecht, G. K. Gupta, H. Y. Zhu, A. M. Dean, R. J. Kee, L. Maier, O. Deutschmann. Methane reforming kinetics within a Ni-YSZ SOFC anode support. *Applied Catalysis A-General* 2005;295(1):40–51.
- [10] V. M. Janardhanan, O. Deutschmann. CFD analysis of a solid oxide fuel cell with internal reforming: Coupled interactions of transport heterogeneous catalysis and electrochemical processes. *J Power Sources* 2006;162:1192–202.
- [11] S. Nagata, A. Momma, T. Kato, Y. Kasuga. Numerical analysis of output characteristics of tubular SOFC with internal reformer. *J Power Sources* 2001;101:60–71.
- [12] G. K. Gupta, E. S. Hecht, H. Y. Zhu, A. M. Dean, R. J. Kee. Gas-phase reactions of methane and natural-gas with air and steam in non-catalytic regions of a solid-oxide fuel cell. *J Power Sources* 2006;156(2):434–47.

- [13] R. Peters, R. Dahl, U. Kluttgen, C. Palm, D. Stolten. Internal reforming of methane in solid oxide fuel cell systems. *J Power Sources* 2002;106(1-2):238–44.
- [14] T. X. Ho, P. Kosinski, A. C. Hoffmann, A. Vik. Numerical modeling of solid oxide fuel cells. *Chem. Eng. Sci.* doi:10.1016/j.ces.2008.07.021.
- [15] V. S. Bagotsky (Ed.). *Fundamentals of Electrochemistry*, 2nd Edition. John Wiley & Sons; 2006. Ch. 6.
- [16] E. Chen. Thermodynamics and electrochemical kinetics. In: G. Hoogers (Ed.). *Fuel Cell Technology Handbook*. CRC Press; 2003. Ch. 3.
- [17] P. Holtappels, L. G. J. De Haart, U. Stimming, I. C. Vinke, M. Mogensen. Reaction of CO/CO₂ gas mixtures on Ni-YSZ cermet electrodes. *J Applied Electrochemistry* 1999;29(5):561–68.
- [18] Y. Matsuzaki, I. Yasuda. Electrochemical oxidation of H₂ and CO in a H₂-H₂O-CO-CO₂ system at the interface of a Ni-YSZ cermet electrode and YSZ electrolyte. *J Electrochemical Society* 2000;147:1530–35.
- [19] A. Weber, B. Sauer, A. C. Muller, D. Herbristrit, E. Ivers-Tiffée. Oxidation of H₂, CO and methane in SOFCs with Ni/YSZ-cermet anodes. *Solid State Ionics* 2002;152(Part A Sp. Iss. SI):543–50.
- [20] Z. Zhan, Y. Lin, M. Pillai, I. Kim, S. A. Barnett. High-rate electrochemical partial oxidation of methane in solid oxide fuel cells. *J Power Sources* 2006;161(1):460–65.
- [21] P. W. Li, M. K. Chyu. Electrochemical and transport phenomena in solid oxide fuel cells. *J Heat Transfer-Transactions of the ASME* 2005;127:1344–62.
- [22] L. M. Raff. *Principles of Physical Chemistry*. Upper Saddle River, NJ: Prentice Hall; 2001.

- [23] H.-T. Lim, A. V. Virkar. Measurement of oxygen chemical potential in thin electrolyte film, anode-supported solid oxide fuel cells. *J Power Sources* 2008;180(1):92–102.
- [24] W. G. Bessler, S. Gewies, M. Vogler. A new framework for physically based modeling of solid oxide fuel cells. *Electrochimica Acta* 2007;53:1782–800.

List of Figures

1	Schematic diagram of a unit planar anode-supported SOFC. The dashed lines indicate the domain of consideration.	32
2	Computational mesh	33
3	Mean gas compositions in the anode channel along the cell length - The co-flow case.	34
4	Mean temperature in the bulk-gas channels and in the electrolyte - The co-flow case.	35
5	Mean temperature in the electrolyte in cases of with and without CO oxidation - The co-flow case.	36
6	Current density along the cell length in cases of with and without CO oxidation - The co-flow case.	37
7	Mean gas compositions in the anode channel along the cell length - The counter-flow case.	38
8	Mean temperature in the bulk-gas channels and in the electrolyte - The counter-flow case.	39
9	Current density along the cell length - The counter-flow case.	40
10	Mean temperature in the electrolyte along the cell length - Air inlet at 1023 K and 1073 K.	41
11	Current density along the cell length - Air inlet at 1023 K and 1073 K.	42
12	Mean temperature in the electrolyte along the cell length - Air inlet velocity -6.3 m/s and -8.3 m/s.	43
13	Current density along the cell length - Air inlet velocity -6.3 m/s and -8.3 m/s.	44

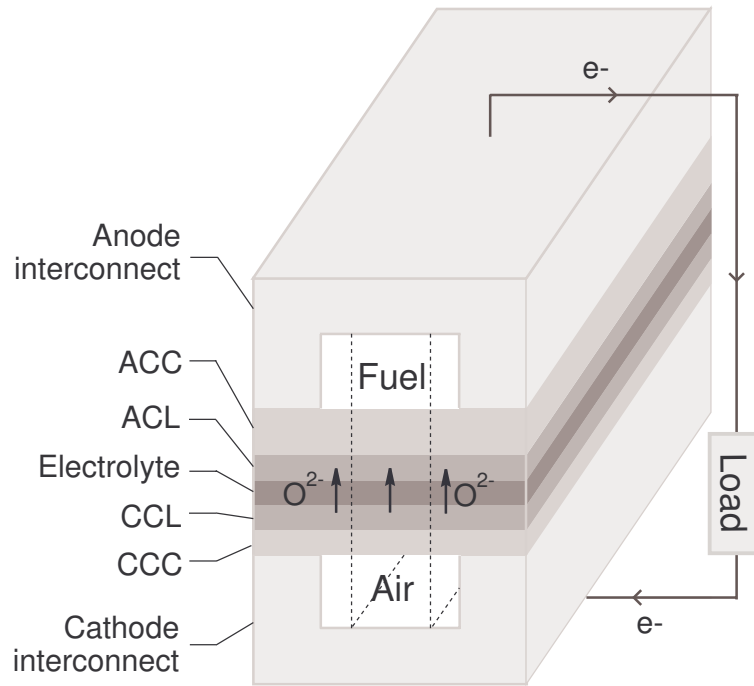


Fig. 1. Schematic diagram of a unit planar anode-supported SOFC. The dashed lines indicate the domain of consideration.

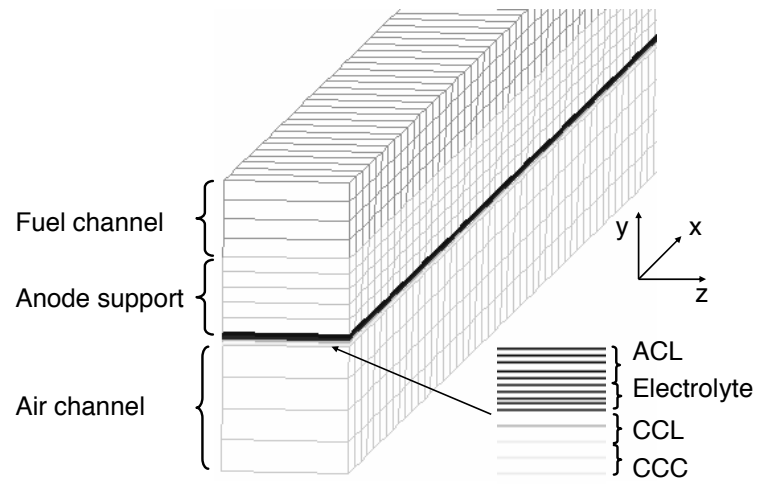


Fig. 2. Computational mesh

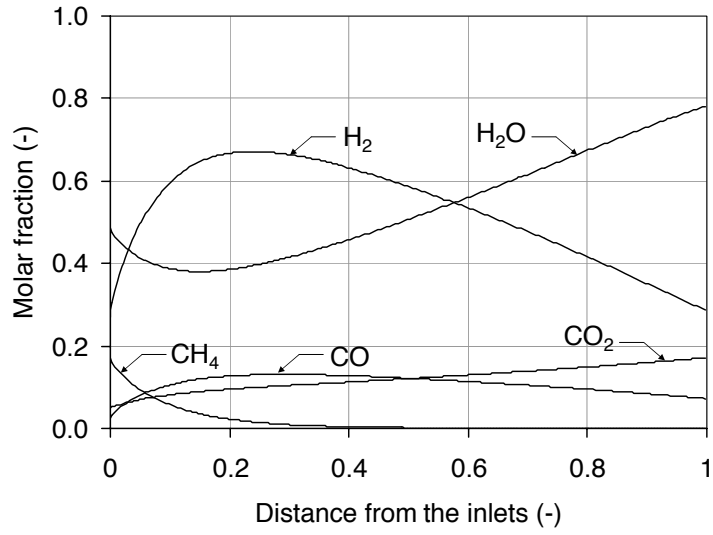


Fig. 3. Mean gas compositions in the anode channel along the cell length - The co-flow case.

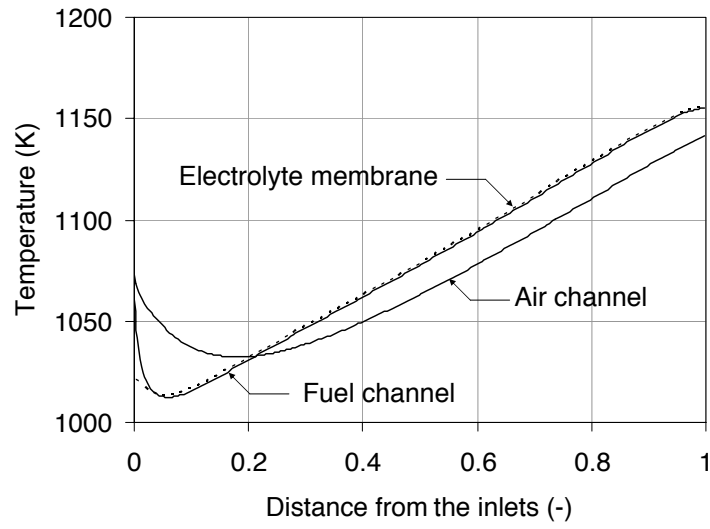


Fig. 4. Mean temperature in the bulk-gas channels and in the electrolyte - The co-flow case.

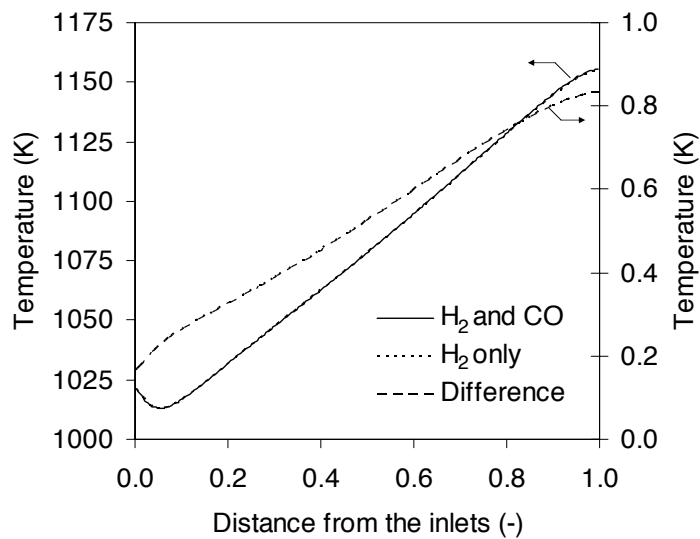


Fig. 5. Mean temperature in the electrolyte in cases of with and without CO oxidation - The co-flow case.

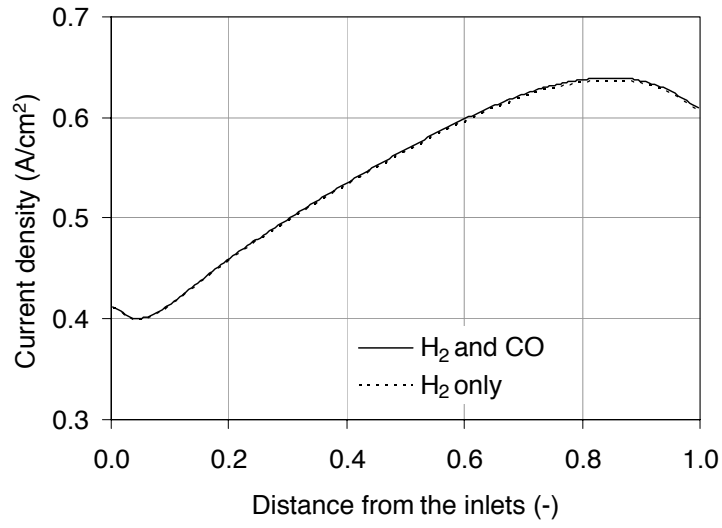


Fig. 6. Current density along the cell length in cases of with and without CO oxidation - The co-flow case.

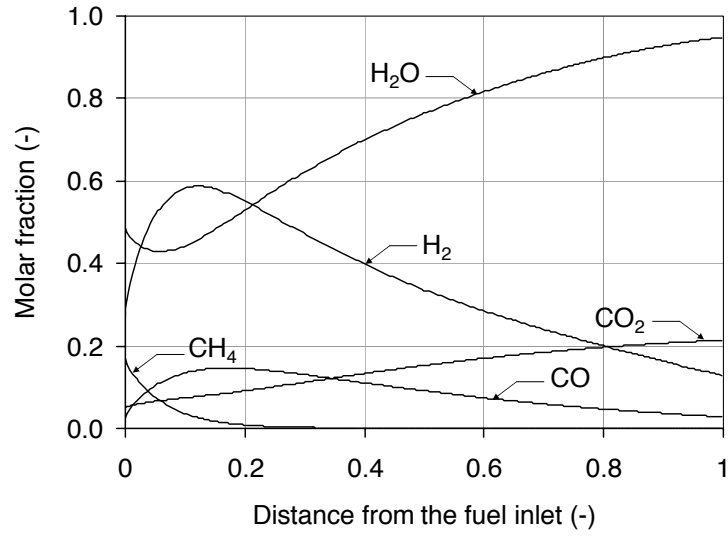


Fig. 7. Mean gas compositions in the anode channel along the cell length - The counter-flow case.

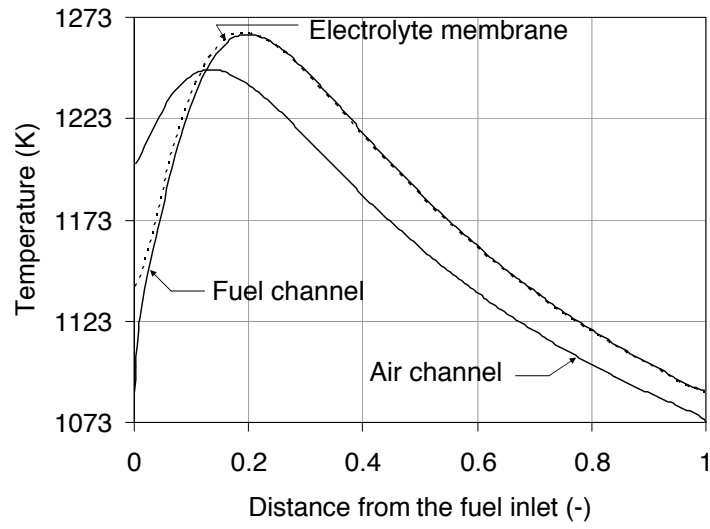


Fig. 8. Mean temperature in the bulk-gas channels and in the electrolyte - The counter-flow case.

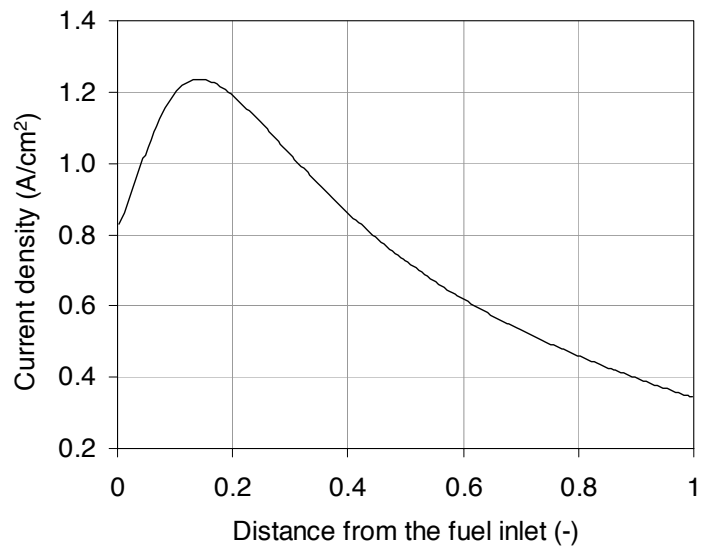


Fig. 9. Current density along the cell length - The counter-flow case.

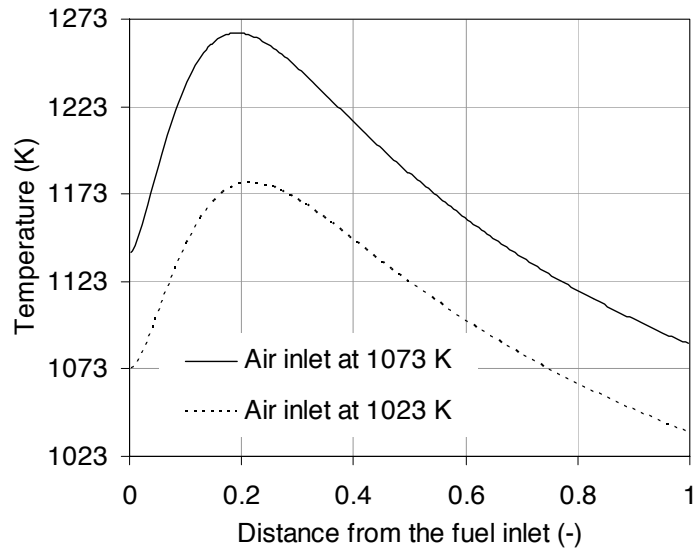


Fig. 10. Mean temperature in the electrolyte along the cell length - Air inlet at 1023 K and 1073 K.

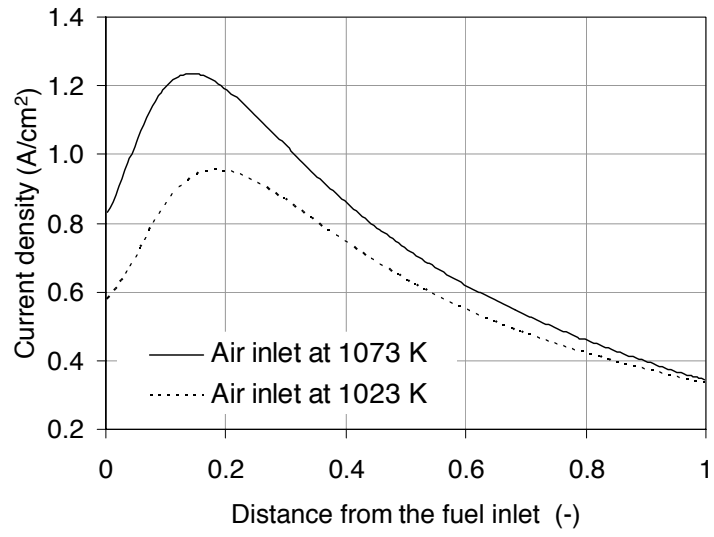


Fig. 11. Current density along the cell length - Air inlet at 1023 K and 1073 K.

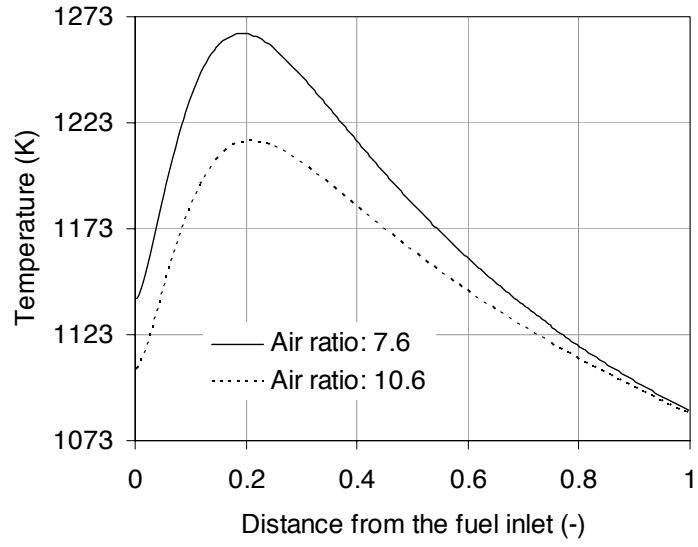


Fig. 12. Mean temperature in the electrolyte along the cell length - Air inlet velocity -6.3 m/s and -8.3 m/s.

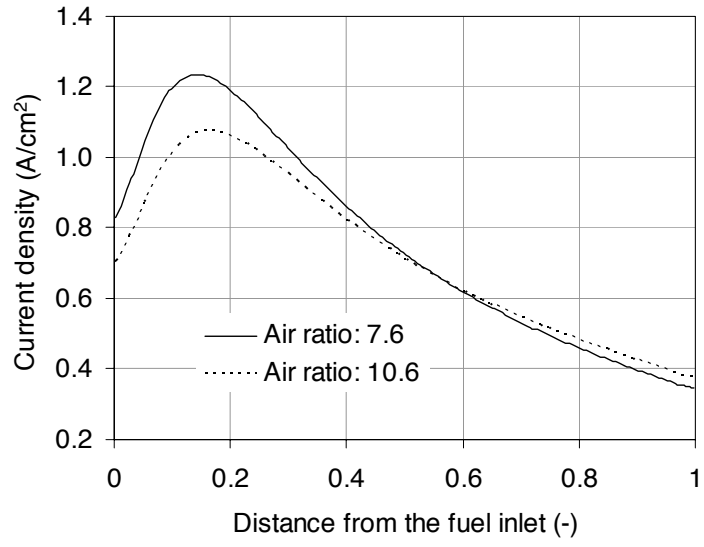


Fig. 13. Current density along the cell length - Air inlet velocity -6.3 m/s and -8.3 m/s.

List of Tables

1	Dimensions and mesh information for the cell components	46
2	Boundary and operating conditions	47
3	Physical properties of cell components	48

Table 1
 Dimensions and mesh information for the cell components

Parameters	Physical dimensions	No. mesh elements
Cell length	100 mm	200
Cell width	1 mm	1
Air channel height	1 mm	4
Fuel channel height	0.6 mm	4
ACC thickness	0.6 mm	5
ACL thickness	30 μm	5
CCL thickness	25 μm	2
CCC thickness	25 μm	2
Electrolyte thickness	20 μm	4

Table 2
Boundary and operating conditions

Parameters	Values and units
Fuel inlet	
Velocity	0.8 m s ⁻¹
Temperature	1073 K
Fuel composition	H ₂ O 48.75%, H ₂ 26.86%, CH ₄ 17.07%, CO 2.40%, CO ₂ 4.91%
Air inlet	
Velocity	6.3 m s ⁻¹
Temperature	1073 K
Air composition	O ₂ 21%, N ₂ 79%
Cell voltage	0.7 V
Rate coefficient, $k_{0,c} = k_{0,a}$	$2.512 \cdot 10^6 \exp(-50000/RT)$

Table 3
Physical properties of cell components

Parameters	Values	Units
Thermal conductivity, k		
Anode/cathode/electrolyte	4/4/10	$\text{W m}^{-1} \text{K}^{-1}$
Oxygen charge diffusion coefficient, D		
in the electrolyte	$0.881\exp(-11000/T)$	$\text{m}^2 \text{s}^{-1}$
Anode/cathode active layer	$0.308\exp(-11000/T)$	$\text{m}^2 \text{s}^{-1}$
Anode/cathode porosity, ϵ	0.4/0.3	
Anode/cathode tortuosity, τ	1.6/1.6	
Anode/cathode pore diameter, d_p	2/1	μm
Anode active layer density (Ni 50%wt.)	4300	kg m^{-3}